Small Structures

small structures

www.small-structures.com

RESEARCH ARTICLE OPEN ACCESS

DNA-Iron Oxide Templated Multifunctional Nanocarbon Networks

Graziano Rilievo[1,2] | Haosen Miao[2] | Aura Cencini[1] | Mary Bortoluzzi[1] | Simone Molinari[3] | Fabio Vianello[1] | Massimiliano Magro[1] | Matteo Palma[2] | Alessandro Cecconello[1,4]

[1]Department of Comparative Biomedicine and Food Science, Università di Padova, Legnaro, Italy | [2]Department of Chemistry, Queen Mary University of London, London, UK | [3]Department of Geosciences, Università di Padova, Padova, Italy | [4]Department of Molecular and Translational Medicine, Università di Brescia, Brescia, Italy

Correspondence: Massimiliano Magro (massimiliano.magro@unipd.it) | Matteo Palma (m.palma@qmul.ac.uk) | Alessandro Cecconello (alessandro.cecconello@unibs.it)

Received: 24 September 2025 | **Revised:** 20 November 2025 | **Accepted:** 24 November 2025

Keywords: carbon nanotubes | DNA | fullerene | graphene | maghemite | optoelectronics

ABSTRACT

The assembly of hybrid nanocomposites often leads to the emergence of new properties. For example, DNA-scaffolded colloidal gold can exhibit chiroplasmonic signals, while nanocomposite-integrated carbon nanotubes display gating properties. Here, we investigate the application of core–shell iron oxide-DNA nanoparticles as a universal nanotechnological "glue" for the fabrication of extended carbon-nanomaterial superstructures. The magnetic nanohybrid, i.e., the nanoglue, is produced by a simple self-assembly process and its properties are tested using three different carbon-based nanomaterials (CBNs): single-wall carbon nanotubes, graphene flakes, and fullerene. In all cases, the generated micrometric architectures integrate the magnetic, optical, and colloidal properties of the nanoglue, further turning water-insoluble CBNs into fully water-dispersible nanocomposites (ca. 1 g L^{-1}), and displaying photoresponsive properties, once organized in a device configuration. Atomic force microscopy and scanning electron microscopy characterizations show distinctive geometries associated with the specific CBN employed. In addition, while Raman spectroscopy investigations demonstrate the hybrid possess increased p-type doping, fluorescence microscopy confirms green light emission. We envision the nanoglue presented in this study to be of general applicability for the construction of a variety of functional CBN architectures toward their potential integration into sensors, nanogates, and nanophotonic devices.

1 | Introduction

The assembly of different nanomaterials into a composite [1, 2] can produce a synergy of properties, not present in the individual components, for a variety of applications ranging from the development of novel architectures for energy-storage and conversion [3–5], to catalysts for green fuel production [6, 7], additive-manufacturing materials [8, 9], and electronic components [10]. For example, carbon-based nanomaterials (CBNs) such as fullerene (C_{60}), carbon nanotubes (CNTs), and graphene flakes (GFs) have been employed to assemble hybrids of particular interest in the context of photon absorption and electron or hole transfer at heterointerfaces, thanks to their electronic properties and their 0D, 1D, and 2D geometries, respectively [11–14]. Nucleic acids, DNA and RNA, have also been used to develop different nanoobjects in solution and on surfaces [15], thanks to their ability to self-assemble by design into duplex-stabilized geometries [16]. Metal, metal oxide, or biomolecular components were integrated into such scaffolds, generating multifunctional materials with specific optical, magnetic, or catalytic properties [17–20].

Notably, DNA and CBN ability to interact via hydrophobic interactions was demonstrated [21, 22], DNA-wrapped CNTs being an example. This approach, based on self-assembly, was further used to develop methodologies to separate different-chirality CNTs

from a mixture, thanks to sequence-specific affinities between single-strand DNA and the CNTs [23–25]. Moreover, approaches to organize CNTs in nano- and microdevices with high precision, by means of DNA tethering, were reported [26, 27].

Bridging CBNs and nanosized metal oxides to produce nanocomposites, on the other hand, commonly requires specific chemistries, as, for example, in situ generation for the production of hybrids comprising CNTs and SPIONs (superparamagnetic iron oxide nanoparticles) for multimodal imaging [28] or (SPION)-C_{60} hybrids obtained by click-chemistry [29]. This is due to the strong hydrophobicity of CBNs, contrasting with the strong hydrophilicity of nanosized metal oxides, which usually expose positive charges on their surface. For this reason, only few examples of nanocomposites combining SPIONs and CBNs were reported [30, 31], with hybrid nanomaterials proposed mainly for biomedical imaging applications [32, 33]. In this context, the development of a general protocol to self-assemble these organic–inorganic hybrids would promote their application in electronic devices, especially for the production of thin conductive films; this would further provide multifunctionality. In addition, the integration of these nanocomposites into stimuli-responsive electronic gates can be expected to generate nano-sized switches for their integration into optoelectronic devices.

In this study, we investigated the role of SAMN@DNA, i.e., single-strand DNA associated with in-house-made SPIONs called Surface-Active Maghemite Nanoparticles (SAMNs), as a nanotechnological "glue" capable of bridging hydrophobic CBNs with magnetic nanoparticles via a general mechanism, turning the system hydrophilic. SAMN@DNA hybrids were already characterized in previous studies where we demonstrated that a stable layer of DNA forms on the iron oxide, with a maximum adsorption capacity equal to 33 mg of DNA per gram of colloidal maghemite, according to the Langmuir model [20, 34]. SAMN and DNA likely interact via phosphate–Fe (III) ion complex formation between the nucleic acid backbone and the nanoparticle surface [34]. We now interfaced these SAMN@DNA hybrids in water with a CBN, promoting interactions between the DNA nucleobase hydrophobic portion (i.e., the portion normally responsible for the base-stacking in duplex DNA) and the CBN surface; this resulted in the formation of a water-dispersible ternary nanomaterial hybrid, thus the term nanoglue. To explore the general applicability of this nanoglue as a linker, three representative CBNs were used: single-wall carbon nanotubes (SWCNTs, called CNTs from here on), graphene flakes (i.e., GFs), and fullerene (i.e., C_{60}).

The self-assembled products were isolated with the aid of an external magnet and extensively characterized using UV–Vis and Raman spectroscopy, scanning electron microscopy (SEM), fluorescence microscopy, and atomic force microscopy (AFM). In addition to providing insights into the ability of the nanoglue to seam nano-objects into complex 3D organizations, we observed distinctive features in the nanocomposites, depending on the carbonaceous material employed. In particular, hydrophobic CNTs gave rise to the formation of stable assemblies, capable of remaining suspended in water for several months. Moreover, as a proof-of-concept study of their applicability as electronic components, we investigated the photocurrent responses, upon illumination, of transistors constructed from the different SAMN@DNA@CBNs. This work introduces a new application of SAMN@DNA, adding a new facet to its affinity for biomolecules [34] and paves the way to an aqueous-based fabrication system of self-assembled DNA-glued hybrid nanomaterials for potential optoelectronic applications.

2 | Results and Discussion

2.1 | Material Fabrication and UV–Vis/NIR Characterization

Single-stranded DNA (ssDNA) was used as a chelating ligand to form a binary hybrid with SAMNs, through an extended *multiple-point-binding* involving the direct interaction of several molecular phosphates from DNA and undercoordinated iron (III) sites on the maghemite nanoparticles surface [35]. The self-assembly process occurred at room temperature for 2 h in aqueous solution (see materials section for additional details and ssDNA sequence), and the as-obtained magnetic nano-bioconjugate (SAMN@DNA) was extensively washed to eliminate loosely bound nucleic acids. SAMN@DNA nanoglue was then used for developing carbon-based nanostructured architectures through a simple self-assembly reaction in water, mediated by the hydrophobic stacking of the DNA nitrogen bases with the hydrophobic CBNs surface (see materials section for additional details) [36].

The general applicability of the nanoglue was tested in combination with three different CBNs: CNTs, GFs, and C_{60}. The synthetic procedure consisted of incubating the nanoglue with the CBN in a NaCl-containing water solution. Graphic layouts of the nanocomplexes and a scheme of the nanohybrid fabrication pipeline are reported in Figure 1, Panels A and B, respectively.

Noteworthy, as a result of a simple incubation with SAMN@DNA in water, almost all the CBN original materials resulted in stable suspensions (ca. 1 g L^{-1} of CBN) and became magnetically responsive. Figure 1C shows photographic pictures of water-suspensions of: the nanoglue (I), the parent CBNs (II, III, and IV), and the final ternary hybrid suspensions (V, VI, and VII, respectively, SAMN@DNA@CNT, SAMN@DNA@GF, and SAMN@DNA@C_{60}), clearly showing a higher degree of acquired colloidal stability associated with the ternary hybrids. Video s1 in the Supporting Information (SI) shows a representative time-lapse of SAMN@DNA@CNT being collected with a permanent magnet.

The unbound carbonaceous material, still present in the supernatant after the self-assembly reaction, was used to quantify the self-assembly process yield by UV–Vis spectroscopy. UV–Vis spectra of SAMN@DNA, each individual CBN, and the nanocomposites are reported in Figure S1, while supernatant spectra after magnetic removal and two washing steps are reported in Figure S2. SAMN@DNA@CNT absorbance appeared to be over-characterized by CNT absorption with two shallow peaks in the IR and UV regions (ca. 1250 nm and 300 nm, respectively, as expected for mixed chirality CNTs employed in this study). On the other hand, the additional two hybrids registered SAMN@DNA absorption as the most relevant contribution at ca. 450 nm (see the experimental section for additional details on CBN features and chirality).

For quantification and colloidal stability test purposes, calibration curves were built by plotting UV–Vis maximum absorbance against CBN concentration (Figure S3). CBN extinction coefficients resulted equal to 4.5 ± 0.6 10^{-3} L mg^{-1} cm^{-1}, 3.5 ±

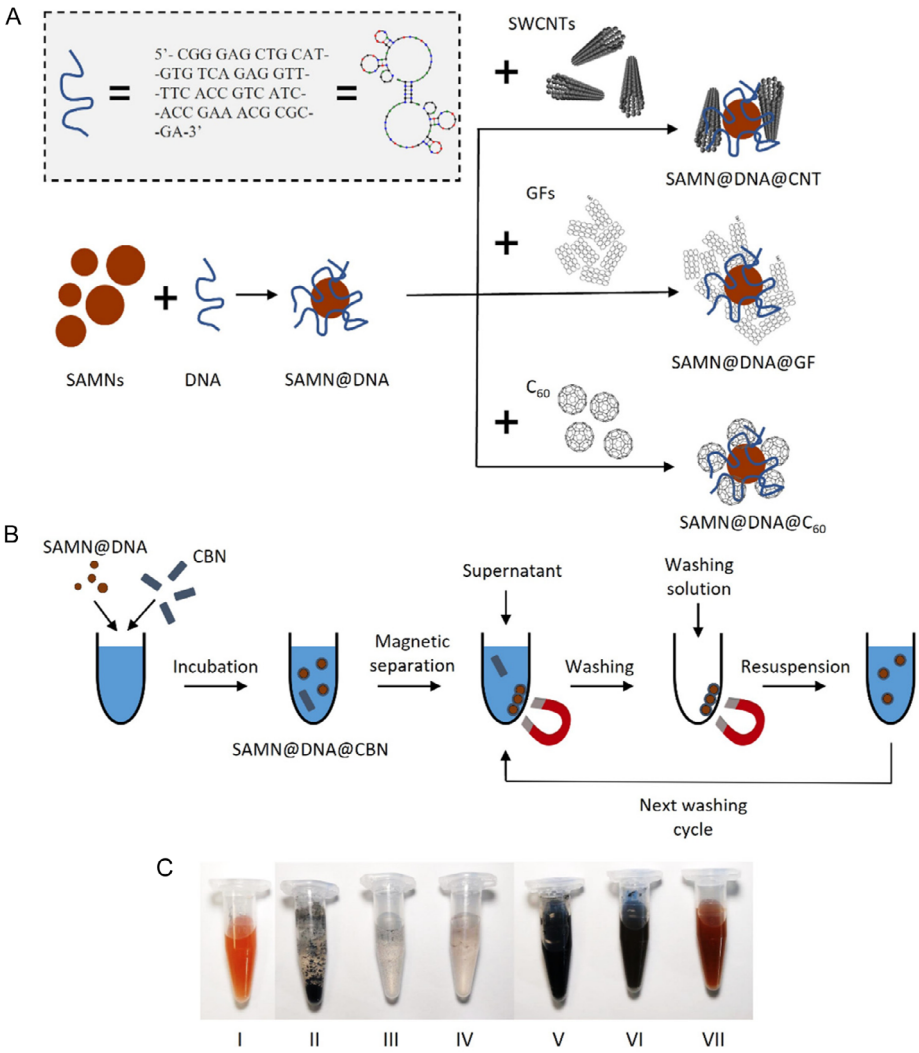

FIGURE 1 | Scheme of nanohybrid fabrication pipeline and hybrid pictures. (A) Hierarchical nanohybrid self-assembly. Inset: Three schematic representations of the ssDNA as a squiggly line, its nucleotide sequence, and its secondary structure generated by nupack.org [37]. (B) Schematic representation of the magnetic separations and washing steps. (C) Pictures of the nanohybrids, the parent CBNs, and SAMN@DNA in water suspension: (I) SAMN@DNA, (II) CNTs, (III) GFs, (IV) C_{60}, (V) SAMN@DNA@CNT, (VI) SAMN@DNA@GF, and (VII) SAMN@DNA@C_{60}.

$0.9\ 10^{-3}$ L mg^{-1} cm^{-1}, and $7.8 \pm 0.9\ 10^{-4}$ L mg^{-1} cm^{-1} for CNT, GF, and C_{60}, respectively. Binding yield calculations also considered the CBN fraction released during the stability tests, which consisted of alternating incubations with fresh 50 mM NaCl solution, under agitation, and magnetic separations until the UV–Vis spectra of the free CBN were zeroed. Noteworthy, the incubation with SAMN@DNA led in all cases to an almost complete suppression of the optical signal related to the free CBN, resulting in magnetic capture yields equal to about 99% for CNTs, 84% for GFs, and 82% for C_{60}, demonstrating the excellent binding ability of SAMN@DNA.

It is worth reporting that for the SAMN@DNA@CNT nanocomplexes, the organic and bioinorganic nanomaterials formed amorphous, microscopic objects (see also video S1), as a result of the SAMN@DNA mediated self-assembly. This magnetically maneuverable material, when isolated from the medium with an external magnet, revealed a mass that was higher than the former nanomaterials used as reagents, and it was attributed to a large amount of structural water incorporated in the hybrid network (ca. 0.97 g g^{-1} as estimated from weighing the pelleted material). The hybrid structure water affinity was further supported by its excellent stability in an aqueous medium (50 mM NaCl solution at neutral pH), showing no sign of precipitation for at least 2 months at 4°C, monitored via UV–Vis spectroscopy. This feature suggests the presence of a 3D network with a specific ratio across the nanocomponents. The next paragraphs report the characterization of such networks.

2.2 | Raman Spectroscopy

A number of Raman signals are particularly interesting for investigating defects in the extended sp^2 structure of CBN: these include the G′ dispersive band, a strong Raman feature exhibited by all kinds of sp^2 carbon materials, that appears in the range 2500–2800 cm^{-1}, and one of the defect main diagnostic signals which is the "disorder-induced" D peak [38], between 1200 cm^{-1} and 1400 cm^{-1}. G′ alterations can be used for monitoring the occurrence of charged defects [39], while the D/G′ intensity ratio was proposed as a parameter to compare defect

density in carbonaceous nanomaterials [40]. An additional disorder-activated band in sp^2 carbon materials is represented by the D′ peak, falling at around 1620 cm^{-1} [41].

Figure 2A shows Raman spectra of bare SAMNs, SAMN@DNA, CNTs, and SAMN@DNA@CNT nanocomposites (datasets I, II, II, and IV, respectively). CNTs are characterized by three main features: the low energy mode at 276 cm^{-1} represents the radial in-phase vibration of the nanotube (i.e., radial breathing mode, RBM) [42]. Vibrations at 1590 and 1546 cm^{-1} are the G_1 and G_2 bands associated with the E_{2g} symmetry of graphite [43, 44], while the feature at 1328 cm^{-1} belongs to the D band. Noteworthy, upon functionalization, G_1 and G_2 bands shifted to slightly lower wavelengths, 1585 and 1539 cm^{-1}, respectively, coupled with an increase of the D band, suggesting an interaction between SAMN@DNA and CNTs (see also peak deconvolution in Figure 2B,C) [45]. In Figure 2D,E, peak deconvolution shows

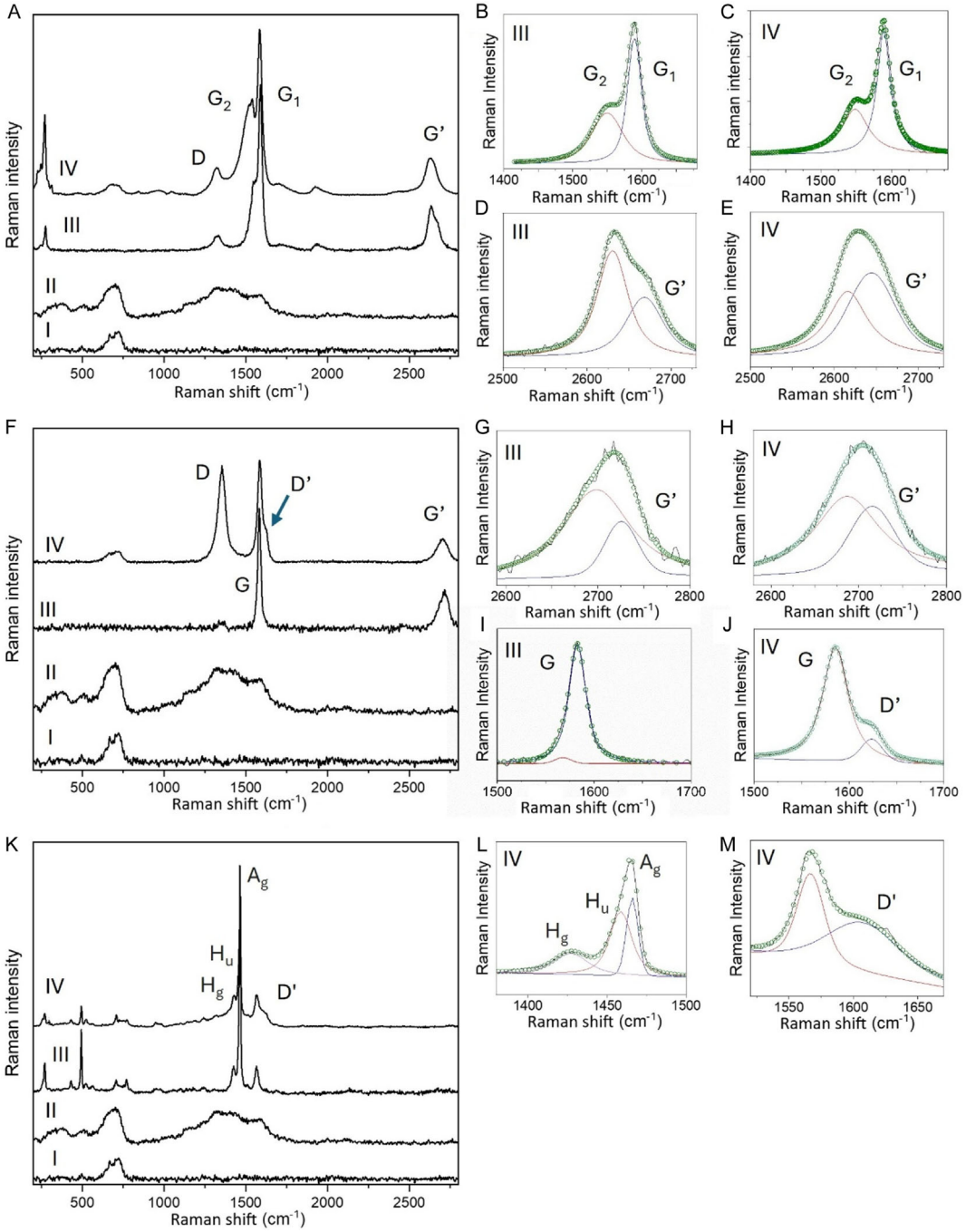

FIGURE 2 | Raman spectroscopy characterization. (A) Spectra corresponding to bare SAMNs, SAMN@DNA, CNTs, and SAMN@DNA@CNT nanocomposites (datasets I, II, III, and IV, respectively). (B–E) Deconvolutions of SAMN@DNA@CNT-associated features shown in A. (F) Spectra corresponding to bare SAMNs, SAMN@DNA, GFs, and SAMN@DNA@GF nanocomposites (datasets I, II, III, and IV, respectively). (G–J) Deconvolutions of SAMN@DNA@GF-associated features shown in F. (K) Spectra corresponding to SAMNs, SAMN@DNA, C_{60}, and SAMN@DNA@C_{60} nanocomposites (datasets I, II, III, and IV, respectively). (L,M) Deconvolutions of SAMN@DNA@C_{60}-associated features shown in K.

that the alteration in the defect-activated G′ band profile can be interpreted as a result of two spectral contributions, with an increase of the signal component at higher wavenumbers in the hybrid. This is likely due to the emergence of additional charge defects upon SAMN@DNA and CNT binding, compatible with CNT p-doping [39]. Indeed, the D/G′ intensity ratio registered a significant 150% increase, indicating that a relevant structural modification accompanied the nanomaterial coupling.

Figure 2F shows the Raman spectra of bare SAMNs, SAMN@DNA, GFs, and SAMN@DNA@GF nanocomposites (datasets I, II, III, and IV, respectively). Graphene clearly exhibits the typical G band at 1585 cm^{-1} related to C=C vibrations of sp^2 domains [46]. Following hybridization, SAMN@DNA@GF nanocomposite still shows main maghemite features in the 600–800 cm^{-1} region while a towering D band at 1355 cm^{-1} appears, hardly detectable in the former carbonaceous nanomaterial and displaying an intensity comparable to the strong G band. Again, the D band was widely described as a disorder- or defect-associated band, indicative of disruptions in graphene aromatic lattice or its oxidation (this band is also associated with the presence of graphene oxide) [46, 47]. Furthermore, similarly to CNT, the G′ feature experienced an alteration as a consequence of hybrid formation. In fact, when compared to the pristine carbonaceous nanomaterial (see peak deconvolution in Figure 2G,H), the profile of the assembly was characterized by a relative increase of the signal component at higher wavenumbers.

D/G′ intensity ratio for this hybrid was calculated to be 8.1, ca. 11-fold higher than the value for the CNT hybrids, pointing to a greater defect density and, therefore, a more relevant structural modification in the GF-based nanohybrids. It is worth mentioning the presence of a peak shoulder close to the G band, identified as the D′ peak [41]. Upon deconvolution, the overlapped signal showed two distinct contributions, the aforementioned G band at 1585 cm^{-1} and, clearly distinguishable, the D′ band at 1626 cm^{-1} (Figure 2I,J).

Figure 2K shows Raman spectra of bare SAMNs, SAMN@DNA, C_{60}, and SAMN@DNA@C_{60} nanocomposites (datasets I, II, III, and IV, respectively). Clearly, SAMN@DNA@C_{60} is dominated by C_{60} features and, in particular, the main peaks centered at 1427, 1464, and 1566 cm^{-1} are assigned to a combination of H_g, H_u, and A_g vibrational modes of fullerene (see also peak deconvolution in Figure 2L) [48, 49]. Although the appearance of the D and G′ peaks was not registered, the presence of a 1566 cm^{-1} peak shoulder mirrors the influence of the interaction with SAMN@DNA on the structural order of the carbon counterpart. As in the previous case, to better appreciate the contribution of the D′ band, the signal was deconvoluted, Figure 2M, revealing a contribution of the disorder-activated band centered at 1620 cm^{-1} and ascribed to the generation of defects due to the hybrid formation process [41].

Overall, hybrid formation induces charge defects in all examined heterostructures. Although the hydrophobic interaction between DNA nitrogenous bases and the carbonaceous components stabilizes the hybrid formation, this can be ruled out as the cause of such structural defects. Defect density for a DNA-modified carbonaceous material was already reported and it was neglectable in comparison to the large D/G′ ratios presented in the current study (see Table 1) [50, 16].

TABLE 1 | Nanomaterial associated D, D′, G′, and D/G′ ratio values.

	Raman intensity		
Nanomaterial	D	G′	D/G′
CNT	12.81	36.6	0.35
SAMN@DNA@CNT	24.09	31.92	0.75
GF	1.78	10.1	0.17
SAMN@DNA@GF	54.3	6.7	8.1

2.3 | SEM

To investigate the microscopic morphology of the nanocomposites, we performed SEM imaging investigations. Figure 3 shows SEM micrographs of the parent CBN components (Panels A, B, and C) and the self-assembled nanocomposites (Panels D, E, and F). It is reasonable to ascribe the observable aggregation, common to all three assemblies and the respective controls, to the sample preparation and the analysis conditions. In fact, the drying process and the vacuum conditions of the microscope are probably responsible for the clamping of the nanocomposites. That said, SEM analysis revealed the presence of sub-micron nanoparticle clusters embedded in all the examined carbonaceous phases, with dimensions ranging from tens to hundreds of nanometers. In SAMN@DNA@CNT (Figure 3D), clusters "islands" (indicated by arrows), likely of iron oxide particles, are visible and surrounded by tightly CNT bundles. This feature can be appreciated for SAMN@DNA@GF as well, although to a minor extent, where the structural features are less heterogeneous (Figure 3E).

2.4 | Confocal Fluorescence Microscopy Imaging

One interesting feature of composite nanomaterials is the possibility to integrate many properties into a product to achieve multifunctionality, without negative effects on the properties of the different components. In this context, to assess whether the luminescence properties of SAMNs (visible emission at ca. 550 nm) were retained in the hybrids, we performed fluorescence microscopy investigations for all three nanocomposites. The materials were visualized with a confocal microscope at 100X magnification, using 488 nm laser excitation wavelength. CBNs are known not to possess a fluorescence signal in the visible range; hence, their possible interferences can be ruled out from the analysis.

Figure 4 shows 1 μm z-stackings of fluorescence images (Panels A), 2D representative areas (Panels B), and selected magnified portions (Panels C), identified by a dotted square in Panel B images. All samples showed emission at 550 nm characteristic of SAMN, with various degrees of heterogeneity (i.e., indicative of structural features). While for SAMN@DNA a rather homogeneous dispersion of signals can be observed, pointing at a nanomaterial that does not form large aggregates and that is therefore lacking superstructures, the presence of extended green regions crossing considerable portions of all the analyzed CBN-comprising hybrids can be appreciated by observing the z-stack representations and the 2D images. Although SEM and fluorescence microscopy are based on different principles, both prompted the presence of a microscopic structural network, particularly in the case of SAMN@DNA@CNT, in which defined anisotropic motifs are

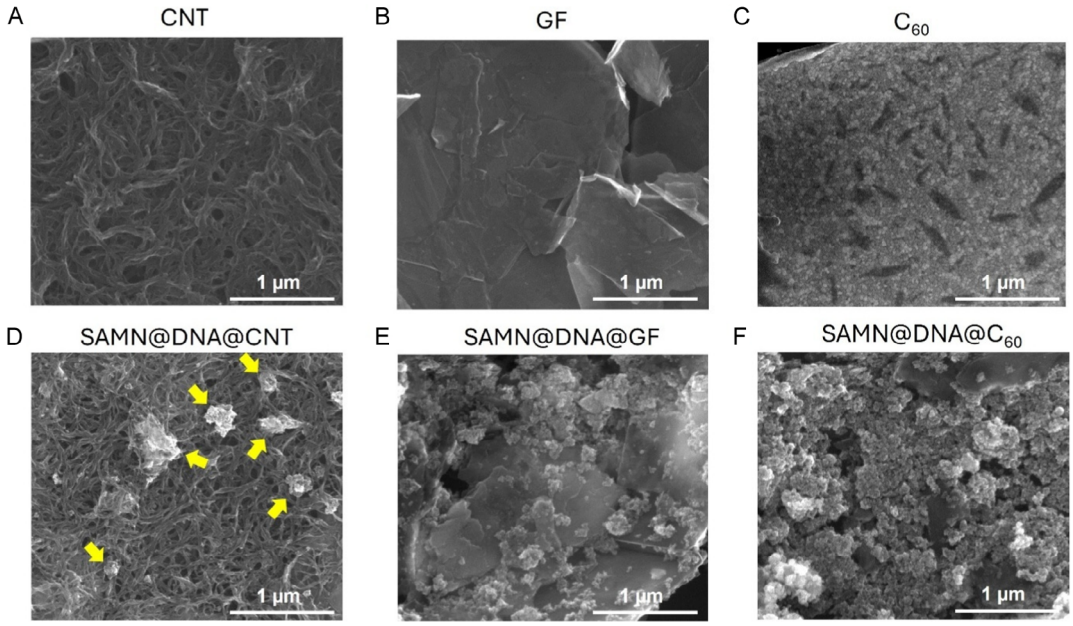

FIGURE 3 | SEM micrographs of films obtained from the three carbon nanomaterials as controls, and the respective ternary nanohybrids built in association with SAMN@DNA. (A) Carbon nanotubes (CNT); (B) graphene flakes (GF); (C) fullerene (C_{60}); (D) SAMN@DNA@CNT; (E) SAMN@DNA@GF; and (F) SAMN@DNA@C_{60}. Arrows point at SAMN@DNA aggregates.

distinguishable. The confocal and SEM micrographs point at a nontrivial spatial organization that extends into the micro-range despite likely being connected via nanojunctions.

2.5 | AFM Characterization

Even though the samples were affected by aggregation phenomena, SEM and confocal microscopy pointed at a certain degree of nanocomposite structural features. We therefore extended our characterizations employing AFM to image in greater detail the different SAMN@DNA@CBNs (the more gentle sample preparation compared to SEM, along with a higher resolution compared to confocal microscopy, should allow us to observe monolayers of the nanocomposites). Representative AFM topographical images of each individual hybrid are reported in Figure 5. SAMN@DNA@CNT hybrids, Figure 5A, are characterized by a network geometry, suggesting a multitude of SAMN@DNA connections among CNTs. The average height of the network was found to be 7 ± 3 nm and the average distance between junctions (i.e., where the network shows a stiff angle) was 500 ± 200 nm (for the individual statistics and fittings, as well as representative cross-section analyses, see the SI, Figure S4 and accompanying text). It is worth mentioning that a different mass ratio in SAMN@DNA@CNT, obtained using a lower concentration of CNTs, resulted in nanocomposites without a clear network structure. AFM characterization and profile analysis are reported in Figure S5, pointing at the critical role of the component ratio.

Similarly, SAMN@DNA@GF profiles are reported in Figure 5B. Quite remarkably, a network analogous to SAMN@DNA@CNT was observed, with spherical nanoparticles ordered in quasilinear assemblies, on top of an island of thin film. Statistical analysis of the network height showed an average value equal to 8 ± 5 nm, which supported the following interpretation: The quasilinear assemblies comprised SAMN@DNA hybrids with an average height equal to 7 ± 3 nm, while the underlying thin material is most probably graphene, with an average height equal to 1.2 ± 0.2 nm (see the SI, Figure S6 and accompanying text for the statistics and fitting of the experimental data, as well as representative cross-section analyses).

Lacking a 1D or 2D component (i.e., CNTs or graphene, respectively), the third nanocomposite, SAMN@DNA@C_{60}, looked rather different from the first two, and AFM images showed concatenation of quasispherical formations clumped in multilayer assemblies. Figure 5C, from left to right, shows increasing magnifications of the same area. Cross-section analysis showed an average height of the aggregates equal to 50 ± 20 nm, while a fine estimate of the smaller-sized objects (13 ± 8 nm) is compatible with individual SAMNs covered with a layer of C_{60} (see the SI, Figure S7 and accompanying text for the statistics and fitting of the experimental data, as well as representative cross-section analyses). For additional details, control AFM profiles of CNTs, graphene, and C_{60}, respectively, along with their associated size distribution statistics, see the SI, Figures S8, S9, and S10 and accompanying text.

Overall, AFM and SEM morphological analyses point to an ordered organization of the nanocomposites, while fluorescence microscopy further demonstrates the integration of fluorescence properties. Moreover, AFM provides solid clues on SAMN@DNA ability to glue CNBs into extended superstructures, with individual features that depend on the parent carbonaceous material, ranging from being markedly network-like in the case of SAMN@DNA@CNT, to less precisely connected sub-micron objects for SAMN@DNA@C_{60}, and with SAMN@DNA@GF being a material with intermediate characteristics.

2.6 | Nanocomposite Photocurrent Response in Devices

Nanostructured materials are particularly attractive for their application as active components in optoelectronic devices [51, 52]. Specifically, CNTs, graphene, and C_{60} were already

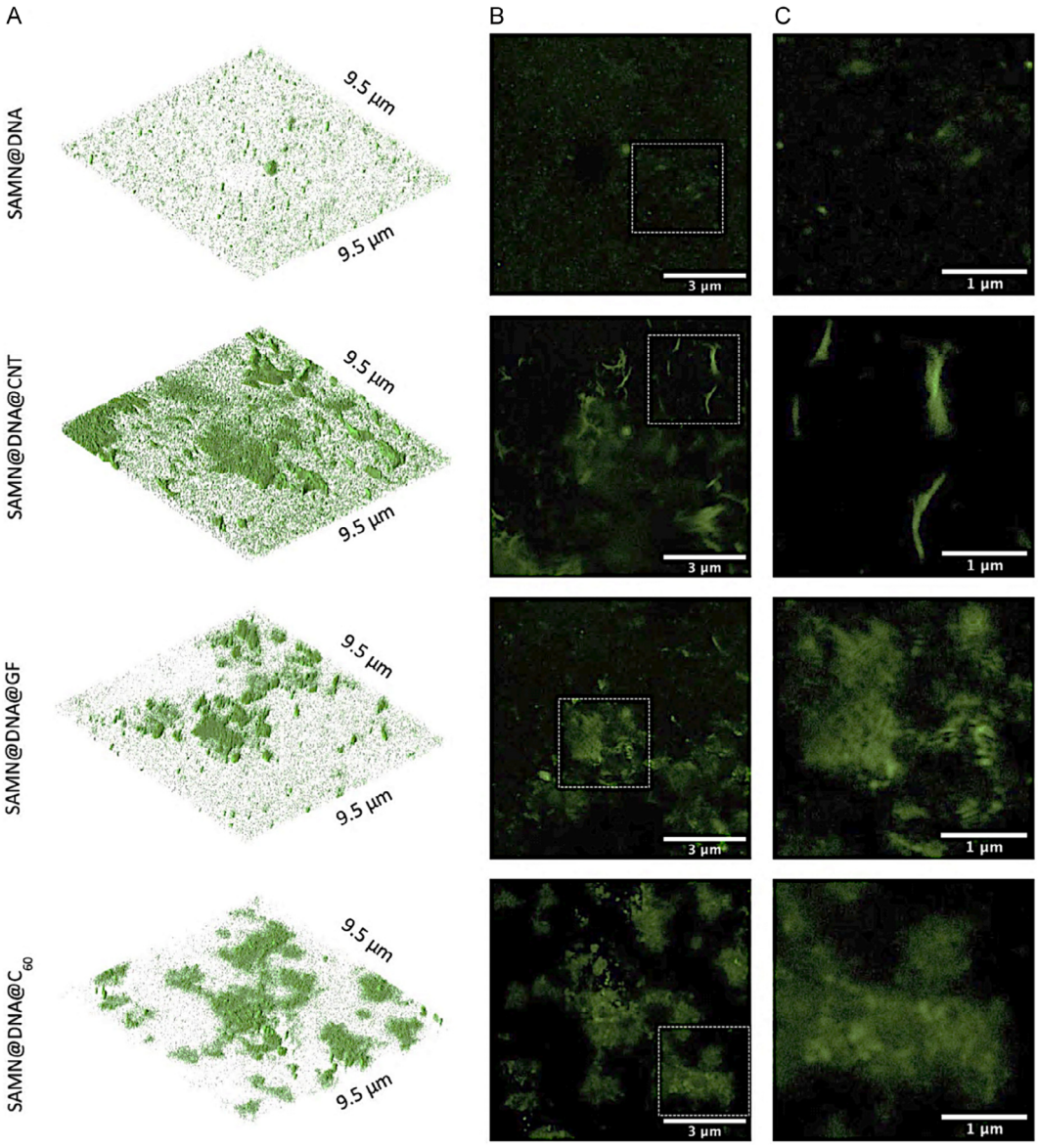

FIGURE 4 | Confocal microscopy images of the control SAMN@DNA and the ternary nanohybrids SAMN@DNA@CNT, SAMN@DNA@GF, and SAMN@DNA@C_{60}. Acquisitions were obtained at 100X magnification objective and digital zoom of 4.32X, with a laser excitation wavelength of 488 nm and detection of emission at 550 nm. (A) z-stack scans of the nanohybrids, collected in a volumetric rendering and projected on an oblique plane with ImageJ software (version 1.53a). In the projection, the z parameter was incremented from 1 µm to 4 µm. (B) 2D images obtained from z-stack optical slices using sum intensity projection with ImageJ software. (C) Magnification of the dotted squares in B to highlight the ternary nanohybrid motifs.

reported as valuable components of such systems and devices [53–55]. The nanocomposites presented here, comprising CBN and SPIONs, could be integrated into (opto)electronic devices, with the added advantage of being processable from aqueous solution. Therefore, we organized the SAMN@DNA@CBNs nanocomposites on prepatterned electrodes in field effect transistor configuration and assessed their photocurrent responses to different illumination wavelengths.

5 µL at 0.5 mg mL^{-1} of the nanocomposite samples (i.e., CNTs, GFs, or C_{60}-comprising SAMN@DNA nanoparticles) were drop-cast on 5 µm-gap interdigitated gold microelectrodes reaching a coverage of ca. 60% (total surface area equal to 35 mm^2) and, as proof of concept, the device electric response was measured upon different illumination cycles (10 mW mm^{-2} laser power). Figure 6A shows a scheme of the set-up where source and drain electrodes are red- and blue- colored, respectively; Figure 6B,C shows two SEM images of a representative nanocomposite (i.e., SAMN@DNA@C_{60}) deposited on interdigitated gold electrodes. The device responses to light were measured as relative current I/I_0, where I_0 is the current recorded at the beginning of the experiment, without illumination, used as a normalizing parameter. Measurements were conducted illuminating with a specific sequence of visible wavelengths, i.e., 405 nm (blue light), 532 nm (green light), or 650 (red light). I/I_0 values were recorded continuously during repeated cycles of illumination (i.e., lamp ON) and dark intervals (i.e., lamp turned OFF), and plotted over time. Figures S11, S12, and S13 further report the gate dependence characterizations carried out by measuring I_{DS} (drain-source current) vs. V_{GS} (gate voltage) curves in the range −10 V to 10 V, with a voltage step of 0.5 V; the results clearly

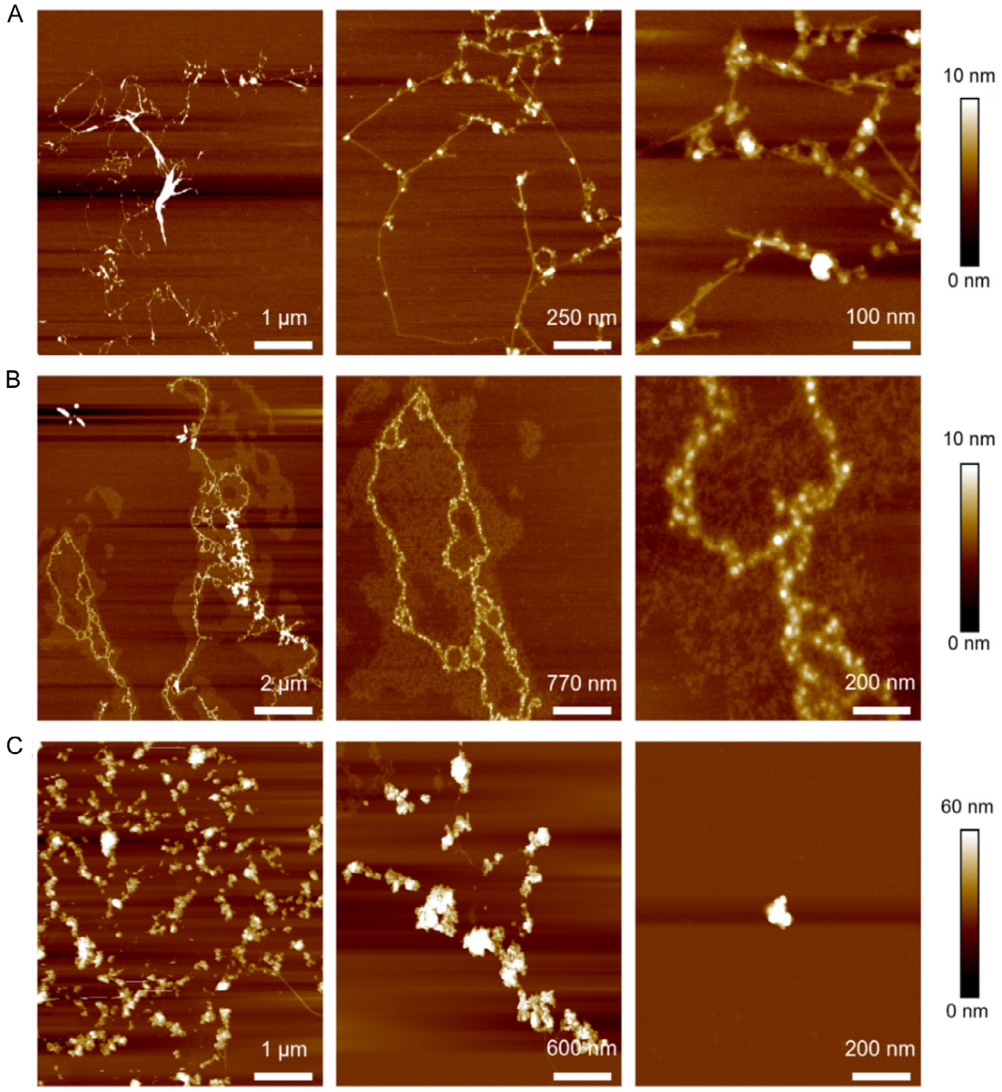

FIGURE 5 | Atomic force microscopy characterization of the nanohybrids deposited on mica. (A) Different magnifications of SAMN@DNA@CNT. (B) Different magnifications of SAMN@DNA@GF. (C) Different magnifications of SAMN@DNA@C_{60}. Images were recorded in air.

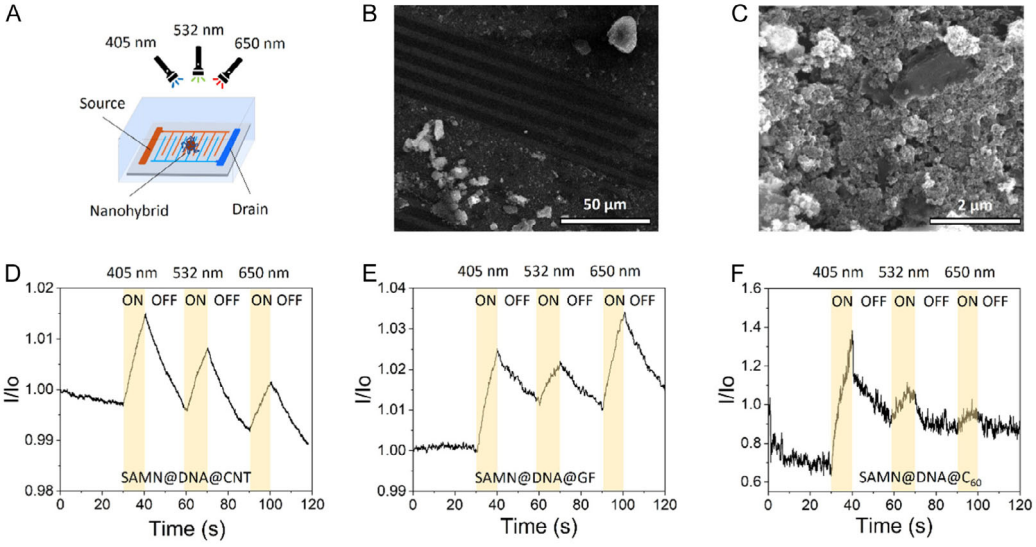

FIGURE 6 | (A) Schematic representation of the device used to record the nanocomposite electrical photocurrent response under different laser illumination wavelengths. (B,C) Representative SEM micrographs of the deposited hybrids on the interdigitated gold microelectrode. (D,E,F) I/I_0 responses of: SAMN@DNA@CNT-modified electrode, SAMN@DNA@GF-modified electrode, and SAMN@DNA@C_{60}-modified electrode.

point to p-type semiconducting behavior of the CBNs and all the nanocomposits.

The photoinduced electrical responses to sequential illuminations were similar for all three nanohybrids, SAMN@DNA@CNT, SAMN@DNA@GF, and SAMN@DNA@C_{60}, respectively, reported in Figure 6D,E,F. The CNT comprising nanocomposite displayed the highest degree of current changes. Furthermore, all the heterostructures showed an increase in the current levels upon illumination, followed by a decrease after the light was turned off. This behavior strongly indicates a photo-induced charge transfer in the organic ternary hybrid, similarly to what we observed in DNA-wrapped CNT-PbS nanohybrids [56], or what has been observed in a ZnO-nanowire/reduced graphene oxide nanocomposite [57]. This proof-of-concept device characterization of the nanoglue hybrids presented here demonstrates their potential for optoelectronic applications.

3 | Conclusion

One attractive facet of nanocomposites is the emergence of non-trivial physical-chemical properties. Here, we showed that a specific SPION-DNA hybrid, i.e., SAMN@DNA, can be used as a universal nanoglue capable of joining water-insoluble CBNs of different geometries (0D, 1D, and 2D) into extended networks by a simple self-assembly process in aqueous solution. While SAMN@DNA was already used for affinity-magnetic purification of biomolecules [34], we extended its use as a crosslinker. Notably, the colloidal stability transferred to nanocarbon materials allowed their dispersion in aqueous solution for solution-processable device integration toward optoelectronic applications.

The general feasibility of the approach was demonstrated by investigating three different CBNs as precursors: CNTs, GF, and C_{60}. Ternary hybrids were successfully developed, with an excellent water solubility (ca. 1 g L^{-1} of CBN) and high colloidal stability (at least 2 months at 4°C for SAMN@DNA@CNT). Their optical, structural, and photoresponsive electric properties were characterized, showing the integration of specific functions from all nanocomponents. Raman spectroscopy indicated the emergence of charge defects (p-doping) on the CBNs upon hybrid formation via the nanoglue. SEM imaging confirmed the formation of networks, while confocal microscopy indicated the retention of SAMN fluorescence properties by all ternary hybrids. AFM results showed in more detail the development of pseudo-ordered micrometric structures, with CNT- and GF-based composites being characterized by extended networks, while SAMN@DNA@C_{60} displayed less defined nanocluster concatenations. This can be intuitively interpreted in terms of a higher proclivity of small 0D particles to behave as nucleation seeds for individual aggregates, while 1D and 2D nanomaterials, such as CNTs and graphene, are geometrically advantaged as building-blocks to develop 3D and branched geometries. Finally, when deposited on an interdigitated gold electrode and illuminated at different wavelengths, the ternary hybrids exhibited photo-induced electrical responses, highlighting their potential use as photoswitchable nanodevices. These results highlight the potential of DNA in the future design of tailored multifunctional superstructures for optoelectronic systems and devices [58, 59], along with its use as a component of carbon-based nanocomposites in electrochemical platforms [60, 61].

4 | Experimental Section

4.1 | Materials

SAMNs were produced with a well-established and patented method (United States Patent US 8,980,218 B2, March 17, 2015). 50-nucleotide ssDNA with sequence: 5′-CGG GAG CTG CAT GTG TCA GAG GTT TTC ACC GTC ATC ACC GAA ACG CGC GA-3′ was purchased from Integrated DNA Technologies (IDT). HiPco CNTs purified SWCNTs (>85%, mixed chirality) were purchased from NanoIntegris. Graphene powder (>95% purity), fullerene powder (C_{60}, 98% purity), NaCl, and $MgCl_2$ were purchased from Sigma Aldrich. Ultrapure water was obtained from a Genie Direct-Pure water device (RephiLe Bioscience). A Nd-Fe-B magnet (N35, 263–287 kJ m^{-3} BH, 1170–1210 mT flux density) was purchased from Power Magnet Shop MTG Europe e.K., Deutschland and was employed for all magnetic separation operations. Acetone and isopropanol solvents were purchased from Sigma Aldrich at the highest grade.

4.2 | UV–Vis, microscopic, AFM, Raman, and SEM characterization

Spectrophotometric analyses were performed with a Cary 60 (Agilent Technologies) UV–Visible spectrophotometer using a 1 cm light path quartz cuvette (Hellma Analytics).

The structure of the ternary hybrids was visualized using a Nikon Ti2 AX-R-NSPARC confocal microscope equipped with a Plan Apo λ 100x/1.45 Oil objective. The acquisition was carried out at an excitation wavelength of 488 nm, with a spatial resolution of 1024 × 1024 pixels and a digital zoom of 4.32X. A z-stack acquisition was performed to enhance the visualization of ternary hybrid structural motifs. For each field acquired, 11 optical slices, scanned every 0.1 µm, were obtained and reconstructed into 3D and 2D images using ImageJ. The brightness and contrast of every z-stack captured were adjusted, keeping the same parameters. The bidimensional images were collected using sum intensity projection, while the 3D images were processed to set up volumetric renderings and visualized in an oblique projection to highlight the ternary hybrids' motifs along inclined planes.

AFM analyses in air were conducted using a Bruker Dimension Icon AFM, in tapping mode with ScanAsyst air tips (tip radius of 12 nm). Bruker Nanoscope Analysis software was used for processing the AFM images. Prior to the analysis, a drop (ca. 10 µL) of 10 mg L^{-1} nanomaterial water suspension was deposited on a freshly cleaved mica, pretreated with 10 mM $MgCl_2$. The samples were then air-dried in a protective atmosphere and scanned once totally dried.

Micro-Raman analyses were carried out using a WITecb Alpha 300R Raman system (WITech GmbH) equipped with a Zeiss microscope and a 532 nm laser operating at a power of 0.3 mW, with a spot diameter of 1.1 µm. Prior to analysis a drop of each sample was deposited on a glass slide and cooled using liquid nitrogen. Spectra were acquired with Control Five software (RWITec) in the range 100–3500 cm^{-1}, with a resolution of 2 cm^{-1}, using 0.2 s of integration time, and 500 accumulations with 300 grooves per mm of grating. The acquired spectra were later processed using Project Five software (RWITec). Peak

deconvolution was carried out using Origin software and assuming Gaussian-shaped peaks.

SEM analyses were performed with a Hitachi 4700 microscope (Hitachi High-Tech Europe) on air dried samples without any derivatization or gold coating. The samples were cast on the support with a concentration of 0.5 mg mL^{-1} and let dry in a protective atmosphere.

4.3 | Illumination-modulated devices photocurrent response

For the electrical photoresponse characterizations, microchips purchased from X Technology UK, with interdigitated 5 X 7 mm, 5 μm gap gold electrodes on SiO_2/Si substrate were employed. The chips were previously washed 10 min in acetone and 10 min in isopropanol, in a sonicating bath (Branson 2800, 110W). After drying them with a gentle argon flux, 5 μL of the samples at a concentration of 0.5 mg mL^{-1} were drop-cast on the electrode surface and air-dried. The so-implemented microchips were then allocated on a PS-100 Probe Station (Lakeshore Cryotronics, Inc., USA) combined with a Keithley 4200SCS semiconducting parameter analyzer (Tektronix UK Ltd.) for electrical characterizations. Measurements were carried out at room temperature. Real-time current measurements were performed by applying a current (I_{DS}) between source (S) and drain electrodes with a constant voltage bias of 0.5 V (no gate voltage applied), and a compliance level of 0.1 A. Three 10 mW mm^{-2} power lasers were used, with wavelengths: 405 nm (blue), 532 nm (green), and 650 nm (red), in a sequential illumination series. The cast nanohybrids were exposed to the light as follows: 30 s of no illumination (baseline current, I_0); 10 s of blue light; 20 s of light-OFF; 10 s of green light; 20 s of light-OFF; 10 s of red light; and a final 20 s of light-OFF (total experiment time 2 min). A baseline current without illumination was also collected for the same time window of the experiment, as no-light exposition control.

Author Contributions

Graziano Rilievo: data curation (lead), formal analysis (lead), investigation (lead), methodology (lead), validation (lead), writing – original draft (supporting). **Haosen Miao:** data curation (supporting), investigation (supporting), methodology (supporting). **Aura Cencini:** data curation (supporting), formal analysis (supporting). **Mary Bortoluzzi:** formal analysis (supporting), investigation (supporting). **Simone Molinari:** data curation (supporting), formal analysis (supporting). **Fabio Vianello:** funding acquisition (equal), supervision (equal). **Massimiliano Magro:** conceptualization (equal), formal analysis (equal), funding acquisition (equal), resources (equal), supervision (equal), writing – original draft (supporting), writing – review and editing (supporting). **Matteo Palma:** conceptualization (equal), resources (equal), supervision (lead), writing – original draft (equal), writing – review and editing (equal). **Alessandro Cecconello:** conceptualization (lead), funding acquisition (equal), project administration (lead), supervision (lead), writing – original draft (lead), writing – review and editing (equal).

Acknowledgments

Graziano Rilievo was supported by The Foundation Blanceflor Boncompagni Ludovisi née Bildt. Aura Cencini was supported by the project animalS and ENvironmenT: toward a sustaINablE Life (SENTINEL) financed by the Italian Ministry of University and Research (MUR) for the period 2023–2027 under the funding scheme "Department of Excellence". Alessandro Cecconello was supported by "Supporting TAlents in ReSearch @ University of Padua – STARS Grants" 2023.

Funding

STARS 2023-Supporting Talents in Research (A. Cecconello), Project: animalS and ENvironmenT: toward a sustaINablE Life (SENTINEL): financed by the Italian Ministry of University and Research (MUR) for the period 2023—2027 under the funding scheme "Department of Excellence" (A. Cencini).

Conflicts of Interest

The authors declare no conflicts of interest.

Data Availability Statement

Additional experimental data can be found in the Supporting Information.

References

1. M. M. Shameem, S. M. Sasikanth, R. Annamalai, and R. Ganapathi Raman, "A Brief Review on Polymer Nanocomposites and its Applications," *Materials Today Proceedings* 45 (2021): 2536–2539.

2. Y. Li, H. Yu, P. Liu, et al., "Photoelectromagnetic Multimode Triggered Phase Change Materials for Thermotherapy," *SusMat* 4 (2024): e214.

3. S. Sekar, A. T. Aqueel Ahmed, S. M. Pawar, et al., "Enhanced Water Splitting Performance of Biomass Activated Carbon-Anchored Wo_3 Nanoflakes," *Applied Surface Science* 508 (2020): 145127.

4. S. Dwivedi, "Solid Oxide Fuel Cell: Materials for Anode, Cathode and Electrolyte," *International Journal of Hydrogen Energy* 45 (2020): 23988-24013.

5. J. Li, G. Wang, L. Yu, et al., "Dual-Functional Template-Induced in Situ Polymerization Process Enables the Hierarchical Carbonaceous Nanotubes with Simultaneous Sn Cluster Incorporation and Nitrogen-Doping for Superior Potassium-Ion Storage," *ACS Applied Materials & Interfaces* 13 (2021): 13139.

6. P. Bharathi, S. Harish, J. Archana, et al., "Enhanced Charge Transfer and Separation of Hierarchical CuO/ZnO Composites: The Synergistic Effect of Photocatalysis for the Mineralization of Organic Pollutant in Water," *Applied Surface Science* 484 (2019): 884.

7. J. Yan, F. Ye, Q. Dai, et al., "Recent Progress in Carbon-based Electrochemical Catalysts: From Structure Design to Potential Applications," *Nano Research Energy* 2 (2023): e9120047.

8. İ. Aktitiz, H. Delibaş, A. Topcu, and K. Aydın, "Morphological, Mechanical, Magnetic, and Thermal Properties of 3D Printed Functional Polymeric Structures Modified with FeO Nanoparticles," *Polymer Composites* 42 (2021): 6839–6846.

9. N. Vidakis, M. Petousis, M. Kourinou, et al., "Additive Manufacturing of Multifunctional Polylactic Acid (PLA)—Multiwalled Carbon Nanotubes (MWCNTs) Nanocomposites" *Nanocomposites* 7 (2021): 184–199.

10. D. Romero-Fierro, M. Bustamante-Torres, F. Bravo-Plascencia, H. Magaña, and E. Bucio, "Polymer-Magnetic Semiconductor Nanocomposites for Industrial Electronic Applications," *Polymers* 14 (2022): 2467.

11. I. V Zaporotskova, N. P. Boroznina, Y. N. Parkhomenko,and L. V Kozhitov, "Carbon Nanotubes: Sensor Properties. A Review" *Modern Electronic Materials* 2 (2016): 95–105.

12. M. S. Arnold, J. L. Blackburn, J. J. Crochet, et al., "Recent Developments in the Photophysics of Single-Walled Carbon Nanotubes for their Use as Active and Passive Material Elements in thin Film

Photovoltaics," *Physical Chemistry Chemical Physics* 15 (2013): 14896–14918.

13. W. A. Gaviria Rojas, and M. C. Hersam, "Chirality-Enriched Carbon Nanotubes for Next-Generation Computing," *Advanced Materials* 32 (2020): 1905654.

14. L. Yu, G. Wang, J. Gao, J. Li, B. Peng, and G. Zhang, "Sacrificial Nanowire Catalyzed Polymerization Process Generates Hierarchical $MoSe_2$ Grafted Carbonaceous Nanotubes for Superior Potassium Ion Storage" *ACS Applied Energy Materials* 4 (2021): 6757–6767.

15. K. M. Kabusure, P. Piskunen, J. J. Saarinen, V. Linko, and T. K. Hakala, "Controlling Raman Enhancement in Particle–Aperture Hybrid Nanostructures by Interlayer Spacing," *Nanoscale* 17 (2025): 3035–3041.

16. M. T. Luu, J. F. Berengut, J. Li, et al., "Reconfigurable Nanomaterials Folded from Multicomponent Chains of Dna Origami Voxels" *Science Robotics* 9 (2024): eadp2309.

17. C. Zhou, X. Duan, and N. Liu, "A Plasmonic Nanorod that Walks on DNA Origami," *Nature Communications* 6 (2015): 8102.

18. A. Kuzyk, R. Schreiber, Z. Fan, et al., "DNA-based Self-Assembly of Chiral Plasmonic Nanostructures with Tailored Optical Response," *Nature* 483 (2012): 311–314.

19. X. Xu, S. Gołębiowska, T. de los Arcos, G. Grundmeier, and A. Keller, "DNA Origami Adsorption at Single-Crystalline TiO_2 Surfaces," *RSC Applied Interfaces* 2 (2025): 931–939.

20. M. Magro, D. Baratella, P. Jakubec, et al., "Triggering Mechanism for DNA Electrical Conductivity: Reversible Electron Transfer between DNA and Iron Oxide Nanoparticles," *Advanced Functional Materials* 25 (2015): 1822–1831.

21. M. Zheng, A. Jagota, M. S. Strano, et al., "Structure-Based Carbon Nanotube Sorting by Sequence-Dependent DNA Assembly," *Science* et al. (2003): 1545.

22. M. Zheng, A. Jagota, E. D. Semke, et al., "DNA-Assisted Dispersion and Separation of Carbon Nanotubes," *Nature Materials* 2 (2003): 338–342.

23. C. M. Sims, M. Zheng, and J. A. Fagan, "Single-Wall Carbon Nanotube Separations via Aqueous Two-Phase Extraction: New Prospects Enabled by High-Throughput Methods," *Chemical Communications* 61 (2025): 2026–2039.

24. X. Tu, S. Manohar, A. Jagota, and M. Zheng, "DNA Sequence Motifs for Structure-Specific Recognition and Separation of Carbon Nanotubes," *Nature* 460 (2009): 250.

25. M. Lyu, B. Meany, J. Yang, Y. Li, and M. Zheng, "Toward Complete Resolution of DNA/Carbon Nanotube Hybrids by Aqueous Two-Phase Systems," *Journal of the American Chemical Society* 141 (2019): 20177.

26. M. Zhao, Y. Chen, K. Wang, et al., "DNA-Directed Nanofabrication of High-Performance Carbon Nanotube Field-Effect Transistors," *Science* 368 (2020): 878–881.

27. W. Sun, J. Shen, Z. Zhao, et al., "Precise Pitch-Scaling of Carbon Nanotube Arrays Within Three-Dimensional DNA Nanotrenches," *Science* 368 (2020): 874–877.

28. J. T. W. Wang, L. Cabana, M. Bourgognon, et al., "Magnetically Decorated Multiwalled Carbon Nanotubes as Dual Mri and Spect Contrast Agents," *Advanced Functional Materials* 24 (2014): 1880.

29. M. Cano, R. Núñez-Lozano, Y. Dumont, C. Larpent, and G. de la Cueva-Méndez, "Synthesis and Characterization of Multifunctional Superparamagnetic Iron Oxide Nanoparticles (SPION)/C60 Nanocomposites Assembled By Fullerene–Amine Click Chemistry," *RSC Advances* 6 (2016): 70374–70382.

30. D. O. Idisi, U. O. Aigbe, C. C. Ahia, and E. L. Meyer, "Graphene Oxide: Fe_2O_3 Nanocomposite: Synthesis, Properties, and Applications," *Carbon Letters* 33 (2023): 605–640.

31. S. Kohzadi, N. Najmoddin, H. Baharifar, and M. Shabani, "Functionalized SPION Immobilized on Graphene-Oxide: Anticancer and Antiviral Study," *Diamond and Related Materials* 127 (2022): 109149.

32. L. Cabana, M. Bourgognon, J. T.-W. Wang, et al., "The Shortening of MWNT-SPION Hybrids by Steam Treatment Improves their Magnetic Resonance Imaging Properties in Vitro and In Vivo," *Small* 12 (2016): 2893–2905.

33. J. T.-W. Wang, C. Fabbro, E. Venturelli, et al., "The Relationship between the Diameter of Chemically-Functionalized Multi-Walled Carbon Nanotubes and their Organ Biodistribution Profiles In Vivo," *Biomaterials* 35 (2014): 9517–9528.

34. A. Cecconello, F. Tonolo, G. Rilievo, et al., "Highly Specific Colloidal γ-Fe_2O_3-DNA Hybrids: From Bioinspired Recognition to Large-Scale Lactoferrin Purification," *Colloids and Surfaces B: Biointerfaces* 234 (2024): 113700.

35. M. Magro, T. Martinello, E. Bonaiuto, et al., "Covalently Bound Dna on Naked Iron Oxide Nanoparticles: Intelligent Colloidal Nano-Vector for Cell Transfection," *Biochimica et Biophysica Acta General Subjects* 1861 (2017): 2802–2810.

36. Y. Li, Y. Wen, L. C. Beltrán, L. Zhu, et al., "Understanding DNA-Encoded Carbon Nanotube Sorting and Sensing Via Sub-nm-Resolution Structural Determination," *Science Advances* 11 (2025): eadt9844.

37. J. N. Zadeh, C. D. Steenberg, J. S. Bois, et al., "NUPACK: Analysis and Design of Nucleic Acid Systems," *Journal of Computational Chemistry* 32 (2011): 170.

38. Y. Wang, Z. Iqbal,and S. V. Malhotra, "Functionalization of Carbon Nanotubes with Amines and Enzymes," *Chemical Physics Letters* 402 (2005): 96.

39. I. O. Maciel, N. Anderson, M. A. Pimenta, et al., "Electron and Phonon Renormalization Near Charged Defects in Carbon Nanotubes," *Nature Materials* 7 (2008): 878.

40. C. Thomsen, and S. Reich, "Raman Scattering in Carbon Nanotubes," *Topics in Applied Physics* 108 (2006): 115.

41. A. C. Ferrari, "Raman Spectroscopy of Graphene And Graphite: Disorder, Electron-Phonon Coupling, Doping and Nonadiabatic Effects," *Solid State Communications* 143 (2007): 47.

42. R. Graupner,"Raman Spectroscopy of Covalently Functionalized Single-Wall Carbon Nanotubes," *Journal of Raman Spectroscopy* 38 (2007): 673-683.

43. G. S. Duesberg, I. Loa, M. Burghard, K. Syassen, and S. Roth, "Polarized Raman Spectroscopy on Isolated Single-Wall Carbon Nanotubes," *Physical Review Letters* 85 (2000): 5436.

44. U. J. Kim, C. A. Furtado, X. Liu, G. Chen, and P. C. Eklund, "Raman and IR Spectroscopy of Chemically Processed Single-Walled Carbon Nanotubes," *Journal of the American Chemical Society* 127 (2005): 15437.

45. S. P. Jovanović, Z. M. Marković, D. N. Kleut, et al., "A Novel Method for the Functionalization of γ-Irradiated Single Wall Carbon Nanotubes with DNA," *Nanotechnology* 20 (2009): 445602.

46. A. Pinilla-Sánchez, E. Chávez-Angel, S. Murcia-López, et al., "Controlling the Electrochemical Hydrogen Generation and Storage in Graphene Oxide by In-Situ Raman Spectroscopy," *Carbon* 200 (2022): 227.

47. A. Sharma, and V. Ramanaiah Dantham, "Observation of Reversible and Irreversible Charge Transfer Processes in Dye-Monolayer Graphene Systems Using Raman Spectroscopy as a Tool," *Spectrochimica Acta Part A: Molecular and Biomolecular Spectroscopy* 317 (2024): 124431.

48. H. Kuzmany, R. Pfeiffer, M. Hulman, and C. Kramberger, "Raman Spectroscopy of Fullerenes and Fullerene–Nanotube Composites" *Philosophical Transactions of the Royal Society of London. Series A: Mathematical, Physical and Engineering Sciences* 362 (2004): 2375.

49. V. Schettino, M. Pagliai, L. Ciabini, and G. Cardini, "The Vibrational Spectrum of Fullerene C60" *Journal of Physical Chemistry A* 105 (2001): 11192.

50. J. R. Simpson, J. A. Fagan, M. L. Becker, E. K. Hobbie, and A. R. Hight Walker, "The Effect of Dispersant on Defects in Length-Separated Single-Wall Carbon Nanotubes Measured by Raman Spectroscopy," *Carbon* 47 (2009): 3238.

51. S. Ge, D. Sang, L. Zou, Y. Yao, et al., "A Review on the Progress of Optoelectronic Devices Based on TiO_2," *Nanomaterials* 13 (2023): 1141.

52. C. Otero-Martínez, N. Fiuza-Maneiro, and L. Polavarapu, "Enhancing the Intrinsic and Extrinsic Stability of Halide Perovskite Nanocrystals for Efficient and Durable Optoelectronics," *ACS Applied Materials & Interfaces* 14 (2022): 34291.

53. Q. B. Zhu, B. Li, D. D. Yang, et al., "A Flexible Ultrasensitive Optoelectronic Sensor Array for Neuromorphic Vision Systems, *Nature Communications* 12 (2021): 1798.

54. J. Yu, X. Yang, G. Gao, Y. Xiong, Y. Wang, J. Han, Y. Chen, H. Zhang, Q. Sun, Z. L. Wang, "Bioinspired Mechano-Photonic Artificial Synapse Based on Graphene/MoS_2 Heterostructure," *Science Advances* 7 (2021): abd9117.

55. E. Meirzadeh, A. M. Evans, M. Rezaee, et al., "A Few-Layer Covalent Network of Fullerenes," *Nature* 613 (2023): 71.

56. Q. Ye, X. Xu, A. Paghi, et al., "Solution-Processable Carbon Nanotube Nanohybrids for Multiplexed Photoresponsive Devices," *Advanced Functional Materials* 31 (2021): 2105719.

57. H. Liu, Q. Sun, J. Xing, et al., "Fast and Enhanced Broadband Photoresponse of a ZnO Nanowire Array/Reduced Graphene Oxide Film Hybrid Photodetector from the Visible to the Near-Infrared Range," *ACS Applied Materials & Interfaces* 7 (2015): 6645–6651.

58. P. L. McMahon, "The Physics of Optical Computing," *Nature Reviews Physics* 5 (2023): 717.

59. T. Fu, J. Zhang, R. Sun, et al., "Optical Neural Networks: Progress and Challenges," *Light, Science & Applications* 13 (2024): 263.

60. Z. Zhu, Y. Men, W. Zhang, et al., "Versatile Carbon-Based Materials from Biomass for Advanced Electrochemical Energy Storage Systems," *eScience* 4 (2024): 100249.

61. J. Li, L. Yu, W. Wang, et al., "Sulfur Incorporation Modulated Absorption Kinetics and Electron Transfer Behavior for Nitrogen Rich Porous Carbon Nanotubes Endow Superior Aqueous Zinc Ion Storage Capability" *Journal of Materials Chemistry A* 10 (2022): 9355.

Supporting Information

Additional supporting information can be found online in the Supporting Information section. **Supporting Video S1:** Magnetic response of SAMN@DNA@CNT. **Supporting Fig. S1:** Optical properties of the three composite materials. UV-Vis absorbance spectra of the ternary hybrids with the respective controls: Panel A - SAMN@DNA@CNT; Panel B - SAMN@DNA@GF; and Panel C - SAMN@DNA@C_{60}. **Supporting Fig. S2:** UV-Vis absorbance spectra of the ternary hybrid supernatant after magnetic removal (sur), washing steps 1 and 2 (wash 1 and wash 2), and the respective CBN, for comparison. Panel A - SAMN@DNA@CNT; Panel B - SAMN@DNA@GF; and Panel C - SAMN@DNA@C_{60}. **Supporting Fig. S3:** UV-Vis calibration curves of the parent carbon-based nanomaterials: Carbon nanotubes (CNTs, Panel A), graphene flakes (GFs, Panel B), and fullerene (C_{60}, Panel C). Calibration curves were used to estimate nanocarbon material concentration in the original incubation suspension and in the supernatant samples, Figure S2. **Supporting Fig. S4:** Statistical analysis of the ternary hybrid SAMN@DNA@CNT height distribution (Panel A) and length distribution (Panel B) using experimental data obtained from AFM analysis (Figure 5A, main text). Panel C: Representative height profiles of the nanohybrid corresponding to the length traces in the AFM image (traces 1, 2, 3, and 4). **Supporting Fig. S5:** AFM analysis of reduced-CNT mass SAMN@DNA@CNT at two different magnifications (Panel A). Panel B: Profile analysis of nanostructures indicated in Panel A. **Supporting Fig. S6:** Statistical analysis of the ternary hybrid SAMN@DNA@GF height distribution (Panel A) and length distribution (Panel B) using experimental data obtained from AFM analysis (Figure 5B, main text). Panel C: Representative height profiles of the nanohybrid corresponding to the length traces in the AFM image (traces 1, 2, and 3). **Supporting Fig. S7:** Statistical analysis of the ternary hybrid SAMN@DNA@C_{60} height distribution (Panel A) and length distribution (Panel B) using experimental data obtained from AFM analysis (Figure 5C, main text). Panel C: Representative height profiles of the nanohybrid corresponding to the length traces in the AFM image (traces 1 and 2). **Supporting Fig. S8:** Statistical analysis of the control CNTs height distribution (Panel A) and length distribution (Panel B) using experimental data obtained from AFM analysis. **Supporting Fig. S9:** Statistical analysis of the control GF height distribution (Panel A) and length distribution (Panel B) using experimental data obtained from AFM analysis. **Supporting Fig. S10:** Statistical analysis of the control C_{60} height distribution using experimental data obtained from AFM analysis. **Supporting Fig. S11:** Current dependence on the gate voltage of the SAMN@DNA nanoconjugate device. Black line: Experimental data; Red line: Exponential fit of the data. **Supporting Fig. S12:** Current dependence on the gate voltage of the (A) SAMN@DNA@CNT, (B) SAMN@DNA@GF, and (C) SAMN@DNA@C_{60} nanohybrids. Black line: Experimental data; Red line: Exponential fit of the data. **Supporting Fig. S13:** Current dependence on the gate voltage of the (A) pristine CNTs, (B) pristine GFs, and (C) pristine C_{60} controls.